

# First measurement of $\nu_e$ and $\bar{\nu}_e$ charged current single charged pion production differential cross sections on argon using the MicroBooNE detector

P. Abratenko,<sup>38</sup> D. Andrade Aldana,<sup>14</sup> L. Arellano,<sup>22</sup> J. Asaadi,<sup>37</sup> A. Ashkenazi,<sup>36</sup> S. Balasubramanian,<sup>12</sup> B. Baller,<sup>12</sup> A. Barnard,<sup>29</sup> G. Barr,<sup>29</sup> D. Barrow,<sup>29</sup> J. Barrow,<sup>26</sup> V. Basque,<sup>12</sup> J. Bateman,<sup>15,22</sup> O. Benevides Rodrigues,<sup>14</sup> S. Berkman,<sup>25</sup> A. Bhat,<sup>7</sup> M. Bhattacharya,<sup>12</sup> M. Bishai,<sup>3</sup> A. Blake,<sup>19</sup> B. Bogart,<sup>24</sup> T. Bolton,<sup>18</sup> M. B. Brunetti,<sup>17,40</sup> L. Camilleri,<sup>10</sup> D. Caratelli,<sup>4</sup> F. Cavanna,<sup>12</sup> G. Cerati,<sup>12</sup> A. Chappell,<sup>40</sup> Y. Chen,<sup>33</sup> J. M. Conrad,<sup>23</sup> M. Convery,<sup>33</sup> L. Cooper-Troendle,<sup>30</sup> J. I. Crespo-Anadón,<sup>6</sup> R. Cross,<sup>40</sup> M. Del Tutto,<sup>12</sup> S. R. Dennis,<sup>5</sup> P. Detje,<sup>5</sup> R. Diurba,<sup>2</sup> Z. Djurcic,<sup>1</sup> K. Duffy,<sup>29</sup> S. Dytman,<sup>30</sup> B. Eberly,<sup>35</sup> P. Englezos,<sup>32</sup> A. Ereditato,<sup>7,12</sup> J. J. Evans,<sup>22</sup> C. Fang,<sup>4</sup> W. Foreman,<sup>14,20</sup> B. T. Fleming,<sup>7</sup> D. Franco,<sup>7</sup> A. P. Furmanski,<sup>26</sup> F. Gao,<sup>4</sup> D. Garcia-Gamez,<sup>13</sup> S. Gardiner,<sup>12</sup> G. Ge,<sup>10</sup> S. Gollapinni,<sup>20</sup> E. Gramellini,<sup>22</sup> P. Green,<sup>29</sup> H. Greenlee,<sup>12</sup> L. Gu,<sup>19</sup> W. Gu,<sup>3</sup> R. Guenette,<sup>22</sup> P. Guzowski,<sup>22</sup> L. Hagaman,<sup>7</sup> M. D. Handley,<sup>5</sup> O. Hen,<sup>23</sup> C. Hilgenberg,<sup>26</sup> G. A. Horton-Smith,<sup>18</sup> A. Hussain,<sup>18</sup> B. Irwin,<sup>26</sup> M. S. Ismail,<sup>30</sup> C. James,<sup>12</sup> X. Ji,<sup>27</sup> J. H. Jo,<sup>3</sup> R. A. Johnson,<sup>8</sup> D. Kalra,<sup>10</sup> G. Karagiorgi,<sup>10</sup> W. Ketchum,<sup>12</sup> M. Kirby,<sup>3</sup> T. Kobilarcik,<sup>12</sup> N. Lane,<sup>15,22</sup> J.-Y. Li,<sup>11</sup> Y. Li,<sup>3</sup> K. Lin,<sup>32</sup> B. R. Littlejohn,<sup>14</sup> L. Liu,<sup>12</sup> W. C. Louis,<sup>20</sup> X. Luo,<sup>4</sup> T. Mahmud,<sup>19</sup> C. Mariani,<sup>39</sup> J. Marshall,<sup>40</sup> N. Martinez,<sup>18</sup> D. A. Martinez Caicedo,<sup>34</sup> S. Martynenko,<sup>3</sup> A. Mastbaum,<sup>32</sup> I. Mawby,<sup>19</sup> N. McConkey,<sup>31</sup> L. Mellet,<sup>25</sup> J. Mendez,<sup>21</sup> J. Micallef,<sup>23,38</sup> A. Mogan,<sup>9</sup> T. Mohayai,<sup>16</sup> M. Mooney,<sup>9</sup> A. F. Moor,<sup>5</sup> C. D. Moore,<sup>12</sup> L. Mora Lepin,<sup>22</sup> M. M. Moudgalya,<sup>22</sup> S. Mulleriababu,<sup>2</sup> D. Naples,<sup>30</sup> A. Navrer-Agasson,<sup>15</sup> N. Nayak,<sup>3</sup> M. Nebot-Guinot,<sup>11</sup> C. Nguyen,<sup>32</sup> J. Nowak,<sup>19</sup> N. Oza,<sup>10</sup> O. Palamara,<sup>12</sup> N. Pallat,<sup>26</sup> V. Paolone,<sup>30</sup> A. Papadopoulou,<sup>1</sup> V. Papavassiliou,<sup>28</sup> H. B. Parkinson,<sup>11</sup> S. F. Pate,<sup>28</sup> N. Patel,<sup>19</sup> Z. Pavlovic,<sup>12</sup> E. Piassetzky,<sup>36</sup> K. Pletcher,<sup>25</sup> I. Pophale,<sup>19</sup> X. Qian,<sup>3</sup> J. L. Raaf,<sup>12</sup> V. Radeka,<sup>3</sup> A. Rafique,<sup>1</sup> M. Reggiani-Guzzo,<sup>11</sup> J. Rodriguez Rondon,<sup>34</sup> M. Rosenberg,<sup>38</sup> M. Ross-Lonergan,<sup>20</sup> I. Safa,<sup>10</sup> D. W. Schmitz,<sup>7</sup> A. Schukraft,<sup>12</sup> W. Seligman,<sup>10</sup> M. H. Shaevitz,<sup>10</sup> R. Sharankova,<sup>12</sup> J. Shi,<sup>5</sup> E. L. Snider,<sup>12</sup> S. Söldner-Rembold,<sup>15</sup> J. Spitz,<sup>24</sup> M. Stancari,<sup>12</sup> J. St. John,<sup>12</sup> T. Strauss,<sup>12</sup> A. M. Szelc,<sup>11</sup> N. Taniuchi,<sup>5</sup> K. Terao,<sup>33</sup> C. Thorpe,<sup>22</sup> D. Torbunov,<sup>3</sup> D. Totani,<sup>4</sup> M. Touns,<sup>12</sup> A. Trettin,<sup>22</sup> Y.-T. Tsai,<sup>33</sup> J. Tyler,<sup>18</sup> M. A. Uchida,<sup>5</sup> T. Usher,<sup>33</sup> B. Viren,<sup>3</sup> J. Wang,<sup>27</sup> M. Weber,<sup>2</sup> H. Wei,<sup>21</sup> A. J. White,<sup>7</sup> S. Wolbers,<sup>12</sup> T. Wongjirad,<sup>38</sup> K. Wresilo,<sup>5</sup> W. Wu,<sup>30</sup> E. Yandel,<sup>4,20</sup> T. Yang,<sup>12</sup> L. E. Yates,<sup>12</sup> H. W. Yu,<sup>3</sup> G. P. Zeller,<sup>12</sup> J. Zennamo,<sup>12</sup> and C. Zhang<sup>3</sup>

(The MicroBooNE Collaboration)\*

<sup>1</sup>Argonne National Laboratory (ANL), Lemont, IL, 60439, USA

<sup>2</sup>Universität Bern, Bern CH-3012, Switzerland

<sup>3</sup>Brookhaven National Laboratory (BNL), Upton, NY, 11973, USA

<sup>4</sup>University of California, Santa Barbara, CA, 93106, USA

<sup>5</sup>University of Cambridge, Cambridge CB3 0HE, United Kingdom

<sup>6</sup>Centro de Investigaciones Energéticas, Medioambientales y Tecnológicas (CIEMAT), Madrid E-28040, Spain

<sup>7</sup>University of Chicago, Chicago, IL, 60637, USA

<sup>8</sup>University of Cincinnati, Cincinnati, OH, 45221, USA

<sup>9</sup>Colorado State University, Fort Collins, CO, 80523, USA

<sup>10</sup>Columbia University, New York, NY, 10027, USA

<sup>11</sup>University of Edinburgh, Edinburgh EH9 3FD, United Kingdom

<sup>12</sup>Fermi National Accelerator Laboratory (FNAL), Batavia, IL 60510, USA

<sup>13</sup>Universidad de Granada, Granada E-18071, Spain

<sup>14</sup>Illinois Institute of Technology (IIT), Chicago, IL 60616, USA

<sup>15</sup>Imperial College London, London SW7 2AZ, United Kingdom

<sup>16</sup>Indiana University, Bloomington, IN 47405, USA

<sup>17</sup>The University of Kansas, Lawrence, KS, 66045, USA

<sup>18</sup>Kansas State University (KSU), Manhattan, KS, 66506, USA

<sup>19</sup>Lancaster University, Lancaster LA1 4YW, United Kingdom

<sup>20</sup>Los Alamos National Laboratory (LANL), Los Alamos, NM, 87545, USA

<sup>21</sup>Louisiana State University, Baton Rouge, LA, 70803, USA

<sup>22</sup>The University of Manchester, Manchester M13 9PL, United Kingdom

<sup>23</sup>Massachusetts Institute of Technology (MIT), Cambridge, MA, 02139, USA

<sup>24</sup>University of Michigan, Ann Arbor, MI, 48109, USA

<sup>25</sup>Michigan State University, East Lansing, MI 48824, USA

<sup>26</sup>University of Minnesota, Minneapolis, MN, 55455, USA

<sup>27</sup>*Nankai University, Nankai District, Tianjin 300071, China*

<sup>28</sup>*New Mexico State University (NMSU), Las Cruces, NM, 88003, USA*

<sup>29</sup>*University of Oxford, Oxford OX1 3RH, United Kingdom*

<sup>30</sup>*University of Pittsburgh, Pittsburgh, PA, 15260, USA*

<sup>31</sup>*Queen Mary University of London, London E1 4NS, United Kingdom*

<sup>32</sup>*Rutgers University, Piscataway, NJ, 08854, USA*

<sup>33</sup>*SLAC National Accelerator Laboratory, Menlo Park, CA, 94025, USA*

<sup>34</sup>*South Dakota School of Mines and Technology (SDSMT), Rapid City, SD, 57701, USA*

<sup>35</sup>*University of Southern Maine, Portland, ME, 04104, USA*

<sup>36</sup>*Tel Aviv University, Tel Aviv, Israel, 69978*

<sup>37</sup>*University of Texas, Arlington, TX, 76019, USA*

<sup>38</sup>*Tufts University, Medford, MA, 02155, USA*

<sup>39</sup>*Center for Neutrino Physics, Virginia Tech, Blacksburg, VA, 24061, USA*

<sup>40</sup>*University of Warwick, Coventry CV4 7AL, United Kingdom*

Understanding electron neutrino interactions is crucial for measurements of neutrino oscillations and searches for new physics in neutrino experiments. We present the first measurement of the flux-averaged  $\nu_e$  and  $\bar{\nu}_e$  charged current single charged pion production cross section on argon using the MicroBooNE detector and data from the NuMI neutrino beam. The total cross section is measured to be  $(0.93 \pm 0.13 \text{ (stat.)} \pm 0.27 \text{ (syst.)}) \times 10^{-39} \text{ cm}^2/\text{nucleon}$  at a mean  $\nu_e$  and  $\bar{\nu}_e$  energy of 730 MeV. Differential cross sections are also reported in electron energy, electron and pion angles, and electron-pion opening angle.

**Introduction.**— The next generation of accelerator neutrino oscillation experiments will seek to address multiple open questions in neutrino physics through precision measurement of electron neutrino appearance in muon neutrino beams. These include the presence and scale of charge-parity violation in the neutrino sector, the neutrino mass hierarchy, and the resolution of anomalies observed at short baselines [1]. Several of these experiments will make use of the liquid argon time projection chamber (LArTPC) detector technology [2, 3]. As such, in order to facilitate these measurements, precise understanding of  $\nu_e$  interactions on argon is essential.

Cross section modeling of  $\nu_e$  interactions is typically extrapolated from  $\nu_\mu$  measurements. However, uncertainties on the  $\nu_e/\nu_\mu$  interaction cross section ratio limit their constraining power [4–7]. Understanding the nuclear effects unique to  $\nu_e$ -argon interactions is crucial for precision neutrino oscillation measurements, rare-event searches, and benchmarking theoretical models used in neutrino experiments.

Reconstructing and measuring  $\nu_e$  interactions also presents unique challenges compared to  $\nu_\mu$  interactions due to the electromagnetic cascades produced by final-state electrons. These are complicated to reconstruct and sensitive to detector calibration uncertainties. Measurements of  $\nu_e$  interactions allow algorithms targeting these topologies to be evaluated and improved reducing systematic uncertainties and enhancing detector performance.

Existing measurements of  $\nu_e$  cross sections on argon are limited consisting of several inclusive measurements [8–10] and a measurement without final state pions [11]. The Deep Underground Neutrino Experiment (DUNE) will be exposed to a neutrino flux peaking at energies of a few GeV [3]. At these energies, one of the dom-

inant neutrino interaction modes leads to the excitation of baryon resonances that subsequently decay producing pions. This process has never previously been measured for  $\nu_e$  interactions.

This work presents the first measurement of the flux-averaged  $\nu_e$  and  $\bar{\nu}_e$  charged-current (CC) single charged pion production cross section on argon using MicroBooNE. The final-state topology considered consists of an electron (or positron), a single charged pion, zero neutral pions (or heavier mesons), and any number of protons or neutrons:

$$\bar{\nu}_e + \text{Ar} \rightarrow e^\pm + 1\pi^\pm + 0\pi^0 + X, \quad (1)$$

where  $X$  represents the residual nucleus and any outgoing nucleons. These interactions will subsequently be referred to as  $\bar{\nu}_e$  CC  $1\pi^\pm$  for simplicity.

The MicroBooNE detector is an 85 tonne LArTPC that collected data between 2015 and 2020. It consists of an instrumented argon volume of  $(2.56 \times 2.32 \times 10.36) \text{ m}^3$  (drift, vertical, beam direction). Ionization charge produced by charged particles resulting from neutrino interactions is drifted towards three planes of readout wires, orientated vertically and at  $\pm 60^\circ$  to the vertical, by an electric field of 273 V/cm. Additionally, scintillation light is collected by an array of 32 photomultiplier tubes located behind the readout planes [12].

MicroBooNE collected data from two neutrino beams: the on-axis 8 GeV Booster Neutrino Beam and the approximately  $8^\circ$  off-axis 120 GeV Neutrinos at the Main Injector (NuMI) beam [13]. In this work, data from the NuMI beam operating in a mixture of forward-horn-current (FHC) neutrino mode and reverse-horn-current (RHC) anti-neutrino mode are used. The NuMI flux at MicroBooNE contains a significant fraction of  $\bar{\nu}_e$  (4%)

due to the high beam energy and the significantly off-axis position of the detector. This makes it particularly useful for  $\bar{\nu}_e$  cross-section measurements. The average  $\bar{\nu}_e$  energies incident on MicroBooNE are 715 MeV in FHC mode and 744 MeV in RHC mode. The integrated exposure is  $8.9 \times 10^{20}$  protons-on-target (POT) in FHC mode and  $11.1 \times 10^{20}$  POT in RHC mode. This corresponds to the full NuMI dataset accumulated by MicroBooNE and used for the first time in this analysis.

At these neutrino energies, the dominant  $\bar{\nu}_e$  CC  $1\pi^\pm$  production mechanism is through the  $\Delta(1232)$  resonance that subsequently decays to a pion and a nucleon. In addition, there are subdominant contributions from coherent pion production and pion production as a result of deep inelastic scattering. The observed topology is also impacted by final-state interactions that can lead to pion production or absorption as the particles produced in the neutrino interaction leave the argon nucleus.

Although pion production has not previously been measured in  $\nu_e$  interactions on argon, it has been probed in  $\nu_\mu$  interactions. ArgoNeuT has performed measurements of  $\nu_\mu$  and  $\bar{\nu}_\mu$  induced charged pion production on argon [14]. MicroBooNE has performed several measurements of  $\nu_\mu$  induced neutral pion production on argon for both CC [15, 16] and neutral-current (NC) interactions [17, 18]. This work presents the first measurement of  $\bar{\nu}_e$  CC  $1\pi^\pm$  on argon. The total interaction cross section is reported along with differential cross sections in electron energy, electron and pion angles, and electron-pion opening angle. These measurements are complementary to the existing suite of  $\bar{\nu}_\mu$  measurements.

**Simulation and reconstruction.**— The NuMI neutrino flux is simulated with GEANT4 v4.10.4 [19–22] constrained with available hadron production data using the PPFX software package [23]. The integrated flux of  $\bar{\nu}_e$  with energy over 60 MeV is  $1.86 \times 10^{-11}/\text{cm}^2/\text{POT}$  in FHC mode and  $1.69 \times 10^{-11}/\text{cm}^2/\text{POT}$  in RHC mode. The combined integrated flux is calculated by weighting the contributions from each horn-current mode according to the accumulated POT in that mode.

The LArSoft software framework [24] is used to perform simulation and reconstruction. Neutrino interactions are modeled using the GENIE v3.0.6 G18.10a.02.11a event generator [25] with the MicroBooNE tune applied [26]. In particular, resonant pion production is simulated using the Kuzmin-Lyubushkin-Naumov Berger-Sehgal model [27–30] and coherent pion production using the Berger-Sehgal model [31]. Propagation of the final state particles through the detector is then performed using GEANT4 [19–21]. This is followed by simulation of the produced ionization electrons and scintillation light and the subsequent detector response [32, 33]. Simulated neutrino interactions are overlaid onto data collected while the beam is off providing data-based modeling of cosmic-

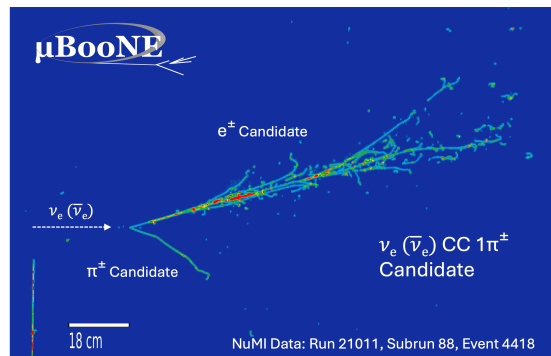


FIG. 1. Event display of a candidate  $\bar{\nu}_e$  CC  $1\pi^\pm$  interaction.

ray induced interactions and detector noise. The Monte-Carlo (MC) prediction consists of simulated neutrino interactions within the detector, simulated interactions upstream of the detector (out-of-cryostat), and data collected with the beam off to model beam spills where no neutrino interaction occurs (EXT).

Reconstruction is performed using the Pandora pattern-recognition toolkit [34]. This uses a multi-algorithm approach to identify neutrino interactions from cosmic-ray-induced backgrounds and to reconstruct each resulting particle. Each particle associated with the neutrino interaction is categorized as a track (muons, pions, protons) or an electromagnetic shower (electrons, photons). Particle identification based on calorimetric and topological information is then performed [35, 36]. Finally, energy reconstruction is performed using particle range for tracks and through calorimetry for showers.

**Signal, selection and observables.**— Signal events are defined as  $\nu_e$  or  $\bar{\nu}_e$  CC interactions that contain an outgoing electron or positron with kinetic energy  $\text{KE}_{e^\pm} > 30$  MeV, a single charged pion with  $\text{KE}_{\pi^\pm} > 40$  MeV, zero neutral pions or heavier mesons, and any number of outgoing protons or neutrons. The signal definition thresholds are guided by the reconstruction thresholds for each particle type. In addition, the opening-angle between the electron and charged pion is required to be  $\theta_{e\pi^\pm} < 170^\circ$ . This removes a region of phase-space, containing less than 0.5% of predicted signal events, for which the reconstruction performance is poor. Figure 1 shows a candidate  $\bar{\nu}_e$  CC  $1\pi^\pm$  interaction matching the signal definition that is selected in MicroBooNE data. A high energy electromagnetic shower is visible along with a single track that is consistent with a charged pion.

The event selection expands upon tools developed in previous MicroBooNE  $\bar{\nu}_e$  analyses [9–11, 37]. Charged current  $\bar{\nu}_e$  interactions are first identified through the presence of an electromagnetic shower consistent with an electron. Tracks present in the event are then assumed to have originated from either protons or charged pions. These are distinguished based on their differing ioniza-

tion profiles or the presence of pion re-interactions. The focus on first identifying charged current  $\bar{\nu}_e$  interactions avoids the need to distinguish between final state muons and charged pions that are otherwise more challenging to separate.

Well-reconstructed candidate events are first identified that have at least one electromagnetic shower and at least one track contained within the instrumented volume. Next, a set of simple cuts are used to remove obvious background events. Cosmic-ray-induced interactions are rejected through *Pandora* classification based on topological characteristics. Electromagnetic showers resulting from neutral pion decays to photons are rejected by applying cuts on three features: the fraction of energy in the leading shower compared to all showers; the shower start position relative to the interaction vertex; and the transverse spread of the shower. Finally,  $\bar{\nu}_e$  interactions containing protons but not pions (referred to subsequently as  $\bar{\nu}_e$  CC Np) are rejected by requiring that at least one track has an ionization profile ( $dE/dx$ ) that is inconsistent with a stopping proton Bragg peak hypothesis [38].

After these initial cuts, more sophisticated methods are applied to refine the event selection further focusing on background suppression through the use of two Boosted Decision Trees (BDTs) trained with *XGBoost* [39]. The BDTs are trained separately for FHC and RHC modes accounting for differences in neutrino composition and energies.

The first BDT focuses on the shower information to distinguish between electrons and photons from neutral pion backgrounds ( $\bar{\nu}_e$  CC  $\pi^0$ ,  $\bar{\nu}_\mu$  CC  $\pi^0$  and NC  $\pi^0$ ). It uses both calorimetric and topological information about the primary shower, any secondary showers if present, and any shower-like clusters of charge identified close to the neutrino interaction.

The second BDT focuses on the track information and aims to distinguish between charged pions and protons, in particular targeting remaining  $\bar{\nu}_e$  CC Np interactions where the proton does not have a clear Bragg peak and, hence, is not rejected at the previous stage. This BDT uses the  $dE/dx$  of the track compared to different particle hypotheses along with topological information focusing on the ends of tracks to identify pion re-interactions or decays. Interactions are selected where only one track is identified as a charged pion candidate, with any number of additional proton candidates allowed.

Figure 2 shows the distribution of scores for the  $\pi^0$ -rejection BDT and  $\bar{\nu}_e$  CC Np-rejection BDT compared with data. The  $\bar{\nu}_e$  CC Np-rejection BDT is shown after the cut on the  $\pi^0$ -rejection BDT has been applied. Both are shown for FHC mode; RHC mode can be found in the Supplemental Material [40]. Both BDTs achieve good signal-background separation for their target topologies. In addition, excellent data-MC agreement within statis-

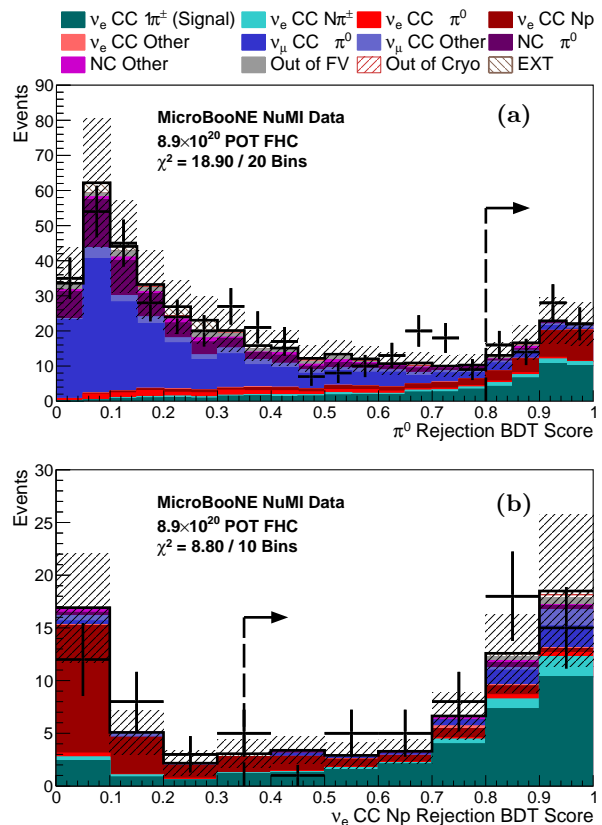


FIG. 2. Distribution of scores for (a) the  $\pi^0$ -rejection BDT and (b) the  $\bar{\nu}_e$  CC Np-rejection BDT compared with FHC mode data. The shaded band shows the systematic and statistical uncertainty on the MC prediction and the black points show the data with statistical uncertainties. The dashed lines show the cuts applied, where events to the right are selected.

tical and systematic uncertainties is seen across the full BDT score distributions.

Candidate  $\bar{\nu}_e$  CC  $\pi^\pm$  interactions are selected with efficiencies of 6.2% and 5.8% and purities of 57.3% and 58.5% for the FHC and RHC beam periods, respectively. In total, 116 candidate events pass the selection in the combined  $2.0 \times 10^{21}$  POT data sample. The selected signal events are predicted to be 78%  $\nu_e$  interactions and 22%  $\bar{\nu}_e$  interactions. They are dominated by resonant production (85%), with smaller contributions from deep-inelastic scattering (11%), quasi-elastic interactions (2%) and coherent interactions (2%).

The observables considered are: the total rate; the electron energy,  $E_e$ ; the electron and pion angles,  $\theta_e$  and  $\theta_\pi$ , with respect to the neutrino direction; and the electron-pion opening angle,  $\theta_{e\pi}$ . Since MicroBooNE is off-axis to the NuMI beam, the exact neutrino direction is not known in data. To reconstruct angles relative to the neutrino direction, neutrinos are assumed to be produced at the NuMI target position. This gives an effective approximation of the neutrino direction with 95% of signal

events having an approximated direction within  $3^\circ$  of the true direction. In simulation, the true direction is known and hence the smearing arising from this approximation can be accounted for during unfolding [10]. Details on the performance of this approximation can be found in the Supplemental Material [40]. The reconstruction resolution is approximately 17% for  $E_e$ , 10% for  $\theta_e$ , 10% for  $\theta_\pi$  and 9% for  $\theta_{e\pi}$ .

Each observable is binned such that there are five bins with approximately ten expected signal events each. In the case of  $E_e$ , the highest energy bin also serves as an overflow bin. For each observable, good data–MC agreement is observed within uncertainties. The selected event distributions can be found in the Supplemental Material [40]

The largest backgrounds are interactions producing neutral pions (13.0% of passing events) and  $\bar{\nu}_e$  CC  $Np$  interactions (11.7% of passing events). Two sidebands are constructed to assess the agreement between data and simulation for these backgrounds. A  $\pi^0$ -rich sideband is constructed by reversing the  $\pi^0$ -rejection BDT cut. This results in a sample with 68.8% purity of  $\pi^0$ -containing interactions with a mixture of  $\bar{\nu}_e$  CC  $\pi^0$ ,  $\bar{\nu}_\mu$  CC  $\pi^0$  and NC  $\pi^0$  topologies. A  $\bar{\nu}_e$  CC  $Np$ -rich sideband is constructed by reversing both the  $\bar{\nu}_e$  CC  $Np$ -rejection BDT cut and the proton Bragg peak cut. This results in a sample with 77.6% purity of  $\bar{\nu}_e$  CC  $Np$  interactions. The level of agreement with data is assessed across each observable considered for both sidebands. Good data–MC agreement is seen across all distributions indicating the background modeling is sufficient to proceed with cross section extraction. The sideband selected event distributions can be found in the Supplemental Material [40].

**Cross section extraction and uncertainties.**— The flux-averaged total cross section and differential cross sections as a function of true kinematic variables are reported. The cross sections are extracted using the Wiener singular value decomposition unfolding technique [41] using a first-derivative regularization term. The impact of the regularization is encoded in a regularization matrix that can be applied to generator predictions to allow direct comparison with the extracted cross sections in the regularized truth space. A block-wise approach to unfolding is used allowing correlations between bins in different variables to be evaluated and reported [42].

Uncertainties on the extracted cross sections are assessed from a variety of sources. The statistical and systematic uncertainties are encoded in a covariance matrix using a block-wise formalism [42]. The total covariance matrix is constructed by summing the covariance matrices of each individual uncertainty.

Systematic uncertainties are considered on: the neutrino flux from hadron production and beam-line geometry modeling [22, 23]; the neutrino interaction cross sec-

tion modeling with GENIE [26]; secondary particle re-interactions [43]; detector response modeling including the scintillation light yield, recombination model, space charge effects [44], and ionization signal response [45]; out-of-cryostat interaction modeling; the number of argon targets; and POT counting. The dominant systematic uncertainty arises from the neutrino flux modeling (20–30%) due to the challenges in simulating the  $8^\circ$  off-axis NuMI beam. This is followed by detector response modeling (15%), predominantly from recombination modeling due to the reliance on calorimetric variables to identify charged pions; and cross section modeling (10%). The other sources of systematic uncertainty are subdominant.

Statistical uncertainties on the data and simulation are evaluated using Poisson uncertainties. Data statistical uncertainties are subdominant for the total cross-section measurement at around 10% but are comparable with systematic uncertainties or dominant for the differential cross-section measurements at around 30%. The total covariance and correlation matrices are reported in the Supplemental Material [40].

The robustness of the unfolding procedure and regularization is assessed using fake data produced by the GENIE and NuWro 19.02.2 [46] generator models. These fake-data tests motivated expanding the cross section modeling uncertainty by treating the NuWro sample as an additional systematic universe [47].

**Results.**— The extracted total cross section is shown in Table I and differential cross sections in  $E_e$ ,  $\theta_e$ ,  $\theta_\pi$  and  $\theta_{e\pi}$  are shown in Fig. 3. The differential cross sections are presented in regularized truth space described by the regularization matrix available in the Supplemental Material [40]. The unfolded data is compared with generator predictions from NuWro 21.09.2 [46], NEUT 5.4.0.1 [48], GiBUU 2025 [49], GENIE 3.0.6 G18\_10a\_02.11a MicroBooNE tune [26] (labeled GENIE 3.0.6 G18 $\mu$ B), and GENIE 3.4.2 AR23\_20i\_00\_000 [25] (labeled GENIE 3.4.2 AR23). Resonant pion production is simulated using the Kuzmin-Lyubushkin-Naumov Berger-Sehgal model [27–30] in GENIE, the Adler-Rarita-Schwinger formalism [50] in NuWro, and the Rein-Sehgal model in NEUT [51]. Coherent pion production is simulated with the Berger-Sehgal [31] model in GENIE, NuWro and NEUT. GiBUU models resonant pion production following the MAID analysis [52] and does not simulate coherent pion production.

The total cross section is measured to be  $(0.93 \pm 0.13$  (stat.)  $\pm 0.27$  (syst.))  $\times 10^{-39}$  cm<sup>2</sup>/nucleon. This is consistent with the predictions from each of the generators considered. The data slightly prefers the higher cross sections predicted by NEUT, NuWro and GiBUU compared with the lower cross sections predicted by GENIE. This could suggest a slight preference for the treatment of resonant pion production or nuclear medium effects in these

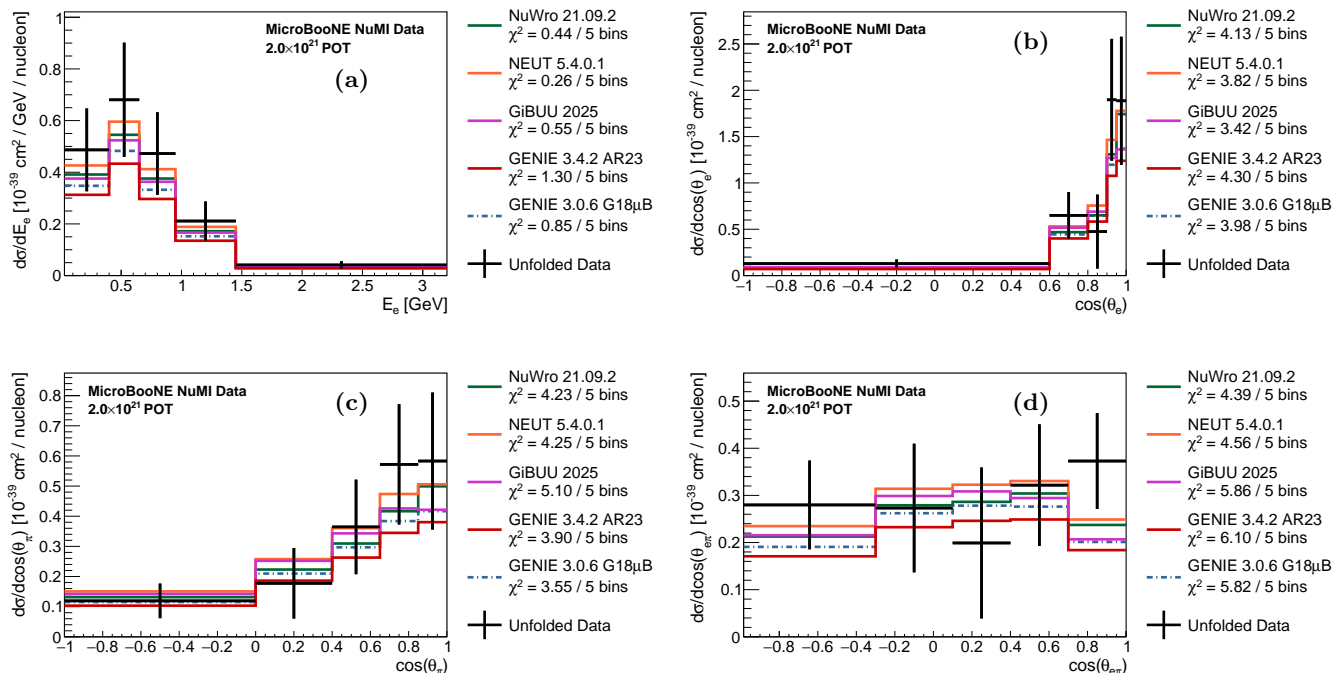


FIG. 3. Extracted differential cross sections in (a) electron energy, (b) electron angle, (c) pion angle and (d) electron-pion opening angle compared with generator predictions. The unfolded data points show both statistical and systematic uncertainties.

Generator	$\sigma$ [ $10^{-39}$ cm <sup>2</sup> /nucleon]	$\chi^2/n_{\text{bins}}$
<b>Unfolded Data</b>	<b><math>0.93 \pm 0.13</math> (stat.) <math>\pm 0.27</math> (syst.)</b>	
NuWro 21.09.2	0.76	0.30/1
NEUT 5.4.0.1	0.83	0.11/1
GiBUU 2025	0.74	0.42/1
GENIE 3.4.0 AR23	0.62	1.11/1
GENIE 3.0.6 G18 $\mu$ B	0.68	0.68/1

TABLE I. Extracted total cross section compared with predictions from generators.

models. However, the sensitivity of the measurement is limited by the large systematic uncertainties on the flux modeling.

The extracted differential cross sections in  $E_e$ ,  $\theta_e$ ,  $\theta_\pi$  and  $\theta_{e\pi}$  are all consistent with the generator predictions. The preference for higher cross sections results in lower  $\chi^2$  for NEUT, NuWro and GiBUU in  $E_e$ ,  $\theta_e$  and  $\theta_{e\pi}$ ; whereas these models have a higher  $\chi^2$  for  $\theta_\pi$  hinting at possible shape disagreement in this variable. The largest  $\chi^2$  are seen for  $\theta_{e\pi}$  driven by the smallest opening angle bin where, in particular, GENIE and GiBUU underpredict the cross section. However, due to the large statistical and flux uncertainties, all models lie within or close to  $1\sigma$  of the data suggesting in general good modeling of this process within the sensitivity of this measurement. To

achieve greater model separation, future measurements would require greater statistics, potentially through improved reconstruction, and improved flux modeling. In particular, additional hadron production data to constrain the off-axis NuMI flux could significantly reduce the associated uncertainties.

**Conclusions.**— We have presented the first measurement of the flux-averaged  $\langle \bar{\nu}_e \rangle_e$  charged current single charged pion production cross section on argon using the MicroBooNE detector. The full NuMI beam data set accumulated by MicroBooNE is used for the first time corresponding to a total exposure of  $2.0 \times 10^{21}$  POT with mean  $\langle \bar{\nu}_e \rangle_e$  energy of 730 MeV. The total cross section is measured to be  $(0.93 \pm 0.13$  (stat.)  $\pm 0.27$  (syst.))  $\times 10^{-39}$  cm<sup>2</sup>/nucleon. Differential cross sections are also reported as functions of electron energy, the electron and pion angles with respect to the neutrino direction, and the electron-pion opening angle. These are found to be in good agreement with generator predictions within uncertainties. This is the first measurement of pion production in  $\langle \bar{\nu}_e \rangle_e$  interactions, one of the dominant interaction modes at the energies of the DUNE neutrino flux. It is essential to understand this process in order to facilitate the DUNE physics program, and direct measurements will have a critical impact to motivate modeling improvements. While this is the first time this process has been measured, the measurement is limited by statistical uncertainties and the challenges

arising from the off-axis flux; future experiments in the SBN program [2] and the DUNE near detector [53] are expected to be able to improve on this.

**Acknowledgments.**— This document was prepared by the MicroBooNE collaboration using the resources of the Fermi National Accelerator Laboratory (Fermilab), a U.S. Department of Energy, Office of Science, Office of High Energy Physics HEP User Facility. Fermilab is managed by Fermi Forward Discovery Group, LLC, acting under Contract No. 89243024CSC000002. MicroBooNE is supported by the following: the U.S. Department of Energy, Office of Science, Offices of High Energy Physics and Nuclear Physics; the U.S. National Science Foundation; the Swiss National Science Foundation; the Science and Technology Facilities Council (STFC), part of the United Kingdom Research and Innovation; the Royal Society (United Kingdom); the UK Research and Innovation (UKRI) Future Leaders Fellowship; and the NSF AI Institute for Artificial Intelligence and Fundamental Interactions. Additional support for the laser calibration system and cosmic ray tagger was provided by the Albert Einstein Center for Fundamental Physics, Bern, Switzerland. We also acknowledge the contributions of technical and scientific staff to the design, construction, and operation of the MicroBooNE detector as well as the contributions of past collaborators to the development of MicroBooNE analyses, without whom this work would not have been possible. For the purpose of open access, the authors have applied a Creative Commons Attribution (CC BY) public copyright license to any Author Accepted Manuscript version arising from this submission.

---

\* microboone.info@fnal.gov

- [1] M. Sajjad Athar *et al.*, Status and perspectives of neutrino physics, *Prog. Part. Nucl. Phys.* **124**, 103947 (2022).
- [2] P. Machado, O. Palamara, and D. W. Schmitz, The Short-Baseline Neutrino Program at Fermilab, *Ann. Rev. Nucl. Part. Sci.* **69**, 363 (2019).
- [3] B. Abi *et al.* (DUNE Collaboration), Long-baseline neutrino oscillation physics potential of the DUNE experiment, *Eur. Phys. J. C* **80**, 978 (2020).
- [4] M. Day and K. S. McFarland, Differences in Quasi-Elastic Cross-Sections of Muon and Electron Neutrinos, *Phys. Rev. D* **86**, 053003 (2012).
- [5] M. Martini *et al.*, Electron-neutrino scattering off nuclei from two different theoretical perspectives, *Phys. Rev. C* **94**, 015501 (2016).
- [6] A. Nikolakopoulos *et al.*, Electron versus Muon Neutrino Induced Cross Sections in Charged Current Quasielastic Processes, *Phys. Rev. Lett.* **123**, 052501 (2019).
- [7] O. Tomalak *et al.*, QED radiative corrections for accelerator neutrinos, *Nature Commun.* **13**, 5286 (2022).
- [8] R. Acciarri *et al.* (ArgoNeuT Collaboration), First measurement of electron neutrino scattering cross section on argon, *Phys. Rev. D* **102**, 011101 (2020).
- [9] P. Abratenko *et al.* (MicroBooNE Collaboration), Measurement of the flux-averaged inclusive charged-current electron neutrino and antineutrino cross section on argon using the NuMI beam and the MicroBooNE detector, *Phys. Rev. D* **104**, 052002 (2021).
- [10] P. Abratenko *et al.* (MicroBooNE Collaboration), First measurement of inclusive electron-neutrino and antineutrino charged current differential cross sections in charged lepton energy on argon in MicroBooNE, *Phys. Rev. D* **105**, L051102 (2022).
- [11] P. Abratenko *et al.* (MicroBooNE Collaboration), Differential Cross Section Measurement of Charged Current  $\nu_e$  Interactions Without Pions in MicroBooNE, *Phys. Rev. D* **106**, L051102 (2022).
- [12] R. Acciarri *et al.* (MicroBooNE Collaboration), Design and Construction of the MicroBooNE Detector, *J. Instrum.* **12**, P02017 (2017).
- [13] P. Adamson *et al.*, The NuMI Neutrino Beam, *Nucl. Instrum. Meth. A* **806**, 279 (2016).
- [14] R. Acciarri *et al.* (ArgoNeuT Collaboration), First measurement of the cross section for  $\nu_\mu$  and  $\bar{\nu}_\mu$  induced single charged pion production on argon using ArgoNeuT, *Phys. Rev. D* **98**, 052002 (2018).
- [15] C. Adams *et al.* (MicroBooNE Collaboration), First measurement of  $\nu_\mu$  charged-current  $\pi^0$  production on argon with the MicroBooNE detector, *Phys. Rev. D* **99**, 091102 (2019).
- [16] P. Abratenko *et al.* (MicroBooNE Collaboration), Measurement of the differential cross section for neutral pion production in charged-current muon neutrino interactions on argon with the MicroBooNE detector, *Phys. Rev. D* **110**, 092014 (2024).
- [17] P. Abratenko *et al.* (MicroBooNE Collaboration), Measurement of neutral current single  $\pi^0$  production on argon with the MicroBooNE detector, *Phys. Rev. D* **107**, 012004 (2023).
- [18] P. Abratenko *et al.* (MicroBooNE Collaboration), First double-differential cross section measurement of neutral-current  $\pi^0$  production in neutrino-argon scattering in the MicroBooNE detector, arXiv:2404.10948 [hep-ex] (2024).
- [19] S. Agostinelli *et al.*, GEANT4—a simulation toolkit, *Nucl. Instrum. Meth. A* **506**, 250 (2003).
- [20] J. Allison *et al.*, Geant4 developments and applications, *IEEE Trans. Nucl. Sci.* **53**, 270 (2006).
- [21] J. Allison *et al.*, Recent developments in Geant4, *Nucl. Instrum. Meth. A* **835**, 186 (2016).
- [22] P. Abratenko *et al.* (MicroBooNE Collaboration), Updates to the NuMI Flux Simulation at MicroBooNE, MICROBOONE-NOTE-1129-PUB (2024).
- [23] L. Aliaga *et al.* (MINERvA Collaboration), Neutrino Flux Predictions for the NuMI Beam, *Phys. Rev. D* **94**, 092005 (2016), [Addendum: *Phys.Rev.D* 95, 039903 (2017)].
- [24] E. Snider and G. Petrillo, LArSoft: Toolkit for Simulation, Reconstruction and Analysis of Liquid Argon TPC Neutrino Detectors, *J. Phys. Conf. Ser.* **898**, 042057 (2017).
- [25] C. Andreopoulos *et al.*, The GENIE Neutrino Monte Carlo Generator, *Nucl. Instrum. Meth. A* **614**, 87 (2010).
- [26] P. Abratenko *et al.* (MicroBooNE Collaboration), New  $CC0\pi$  GENIE model tune for MicroBooNE, *Phys. Rev. D* **105**, 072001 (2022).

- [27] J. A. Nowak (MiniBooNE Collaboration), Four Momentum Transfer Discrepancy in the Charged Current  $\pi^+$  Production in the MiniBooNE: Data vs. Theory, AIP Conf. Proc. **1189**, 243 (2009).
- [28] K. S. Kuzmin, V. V. Lyubushkin, and V. A. Naumov, Lepton polarization in neutrino nucleon interactions, Mod. Phys. Lett. A **19**, 2815 (2004).
- [29] C. Berger and L. Sehgal, Lepton mass effects in single pion production by neutrinos, Phys. Rev. D **76**, 113004 (2007).
- [30] K. M. Graczyk and J. T. Sobczyk, Form Factors in the Quark Resonance Model, Phys. Rev. D **77**, 053001 (2008), [Erratum: Phys.Rev.D 79, 079903 (2009)].
- [31] C. Berger and L. M. Sehgal, Partially conserved axial vector current and coherent pion production by low energy neutrinos, Phys. Rev. D **79**, 053003 (2009).
- [32] C. Adams *et al.* (MicroBooNE Collaboration), Ionization electron signal processing in single phase LArTPCs. Part I. Algorithm Description and quantitative evaluation with MicroBooNE simulation, J. Instrum. **13**, P07006 (2018).
- [33] C. Adams *et al.* (MicroBooNE Collaboration), Ionization electron signal processing in single phase LArTPCs. Part II. Data/simulation comparison and performance in MicroBooNE, J. Instrum. **13**, P07007 (2018).
- [34] R. Acciarri *et al.* (MicroBooNE Collaboration), The Pandora multi-algorithm approach to automated pattern recognition of cosmic-ray muon and neutrino events in the MicroBooNE detector, Eur. Phys. J. C **78**, 82 (2018).
- [35] C. Adams *et al.* (MicroBooNE Collaboration), Calibration of the charge and energy loss per unit length of the MicroBooNE liquid argon time projection chamber using muons and protons, J. Instrum. **15**, P03022 (2020).
- [36] C. Adams *et al.* (MicroBooNE Collaboration), Reconstruction and Measurement of  $\mathcal{O}(100)$  MeV Energy Electromagnetic Activity from  $\pi^0 \rightarrow \gamma\gamma$  Decays in the MicroBooNE LArTPC, J. Instrum. **15**, P02007 (2020).
- [37] P. Abratenko *et al.* (MicroBooNE Collaboration), Search for an anomalous excess of charged-current  $\nu e$  interactions without pions in the final state with the MicroBooNE experiment, Phys. Rev. D **105**, 112004 (2022).
- [38] P. Abratenko *et al.* (MicroBooNE Collaboration), Calorimetric classification of track-like signatures in liquid argon TPCs using MicroBooNE data, J. High Energy Phys. **12**, 153 (2021).
- [39] T. Chen and C. Guestrin, XGBoost: A Scalable Tree Boosting System, in *Proceedings of the 22nd ACM SIGKDD International Conference on Knowledge Discovery and Data Mining* (2016) p. 785–794.
- [40] See Supplemental Material for reverse horn current mode data BDT score distributions, the performance of the reconstructed neutrino direction approximation, the signal region and sideband selected distributions, the unfolded differential cross-section covariance, correlation and regularization matrices and the tabulated results.
- [41] W. Tang, X. Li, X. Qian, H. Wei, and C. Zhang, Data Unfolding with Wiener-SVD Method, J. Instrum. **12**, P10002 (2017).
- [42] S. Gardiner, Mathematical methods for neutrino cross-section extraction, arXiv:2401.04065 [hep-ex] (2024).
- [43] J. Calcutt, C. Thorpe, K. Mahn, and L. Fields, Geant4Reweight: a framework for evaluating and propagating hadronic interaction uncertainties in Geant4, J. Instrum. **16**, P08042 (2021).
- [44] P. Abratenko *et al.* (MicroBooNE Collaboration), Measurement of space charge effects in the MicroBooNE LArTPC using cosmic muons, J. Instrum. **15**, P12037 (2020).
- [45] P. Abratenko *et al.* (MicroBooNE Collaboration), Novel approach for evaluating detector-related uncertainties in a LArTPC using MicroBooNE data, Eur. Phys. J. C **82**, 454 (2022).
- [46] T. Golan, C. Juszczak, and J. T. Sobczyk, Final State Interactions Effects in Neutrino-Nucleus Interactions, Phys. Rev. C **86**, 015505 (2012).
- [47] P. Abratenko *et al.* (MicroBooNE Collaboration), Multidifferential cross section measurements of  $\nu_\mu$ -argon quasielasticlike reactions with the MicroBooNE detector, Phys. Rev. D **108**, 053002 (2023).
- [48] Y. Hayato and L. Pickering, The NEUT neutrino interaction simulation program library, Eur. Phys. J. ST **230**, 4469 (2021).
- [49] O. Buss *et al.*, Transport-theoretical Description of Nuclear Reactions, Phys. Rept. **512**, 1 (2012).
- [50] K. M. Graczyk, D. Kielczewska, P. Przewlocki, and J. T. Sobczyk,  $C(5)^{**A}$  axial form factor from bubble chamber experiments, Phys. Rev. D **80**, 093001 (2009).
- [51] D. Rein and L. M. Sehgal, Neutrino Excitation of Baryon Resonances and Single Pion Production, Annals Phys. **133**, 79 (1981).
- [52] U. Mosel, Neutrino event generators: foundation, status and future, J. Phys. G **46**, 113001 (2019).
- [53] A. Abed Abud *et al.* (DUNE Collaboration), Deep Underground Neutrino Experiment (DUNE) Near Detector Conceptual Design Report, Instruments **5**, 31 (2021).



## Supplemental material

### REVERSE-HORN-CURRENT BDT SCORE DISTRIBUTIONS

Figure 1 shows the distribution of scores for the  $\pi^0$ -rejection BDT and the  $\bar{\nu}_e$  CC Np-rejection BDT compared with data for reverse-horn-current (RHC) mode. The  $\bar{\nu}_e$  CC Np-rejection BDT is shown after the cut on the  $\pi^0$ -rejection BDT has been applied. Both BDTs achieve good signal-background separation for their target topologies. In addition, excellent data–MC agreement within statistical and systematic uncertainties is seen across the full BDT score distributions.

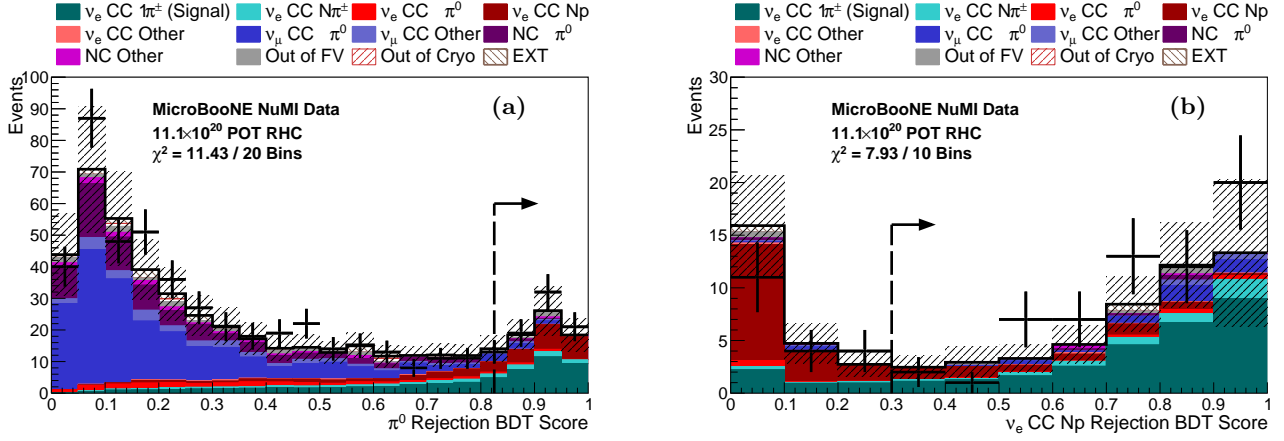


FIG. 1. Distribution of scores for (a) the  $\pi^0$ -rejection BDT and (b) the  $\bar{\nu}_e$  CC Np-rejection BDT compared with RHC mode data. The shaded band shows the systematic and statistical uncertainty on the MC prediction and the black points show the data with statistical uncertainties. The dashed lines show the cuts applied, where events to the right are selected.

## NEUTRINO DIRECTION APPROXIMATION

As a result of the NuMI beam being off-axis to the MicroBooNE detector, neutrinos can arrive at MicroBooNE with a range of directions depending on where along the beam line they are produced. Figure 2 shows the angular distribution of signal  $\bar{\nu}_e$  CC  $1\pi^\pm$  interactions for forward horn current (FHC) mode and RHC mode. The majority are produced close to the NuMI target approximately  $8^\circ$  off-axis. However, a subset are produced at larger off-axis angles as a result of meson decays further along the NuMI decay pipe.

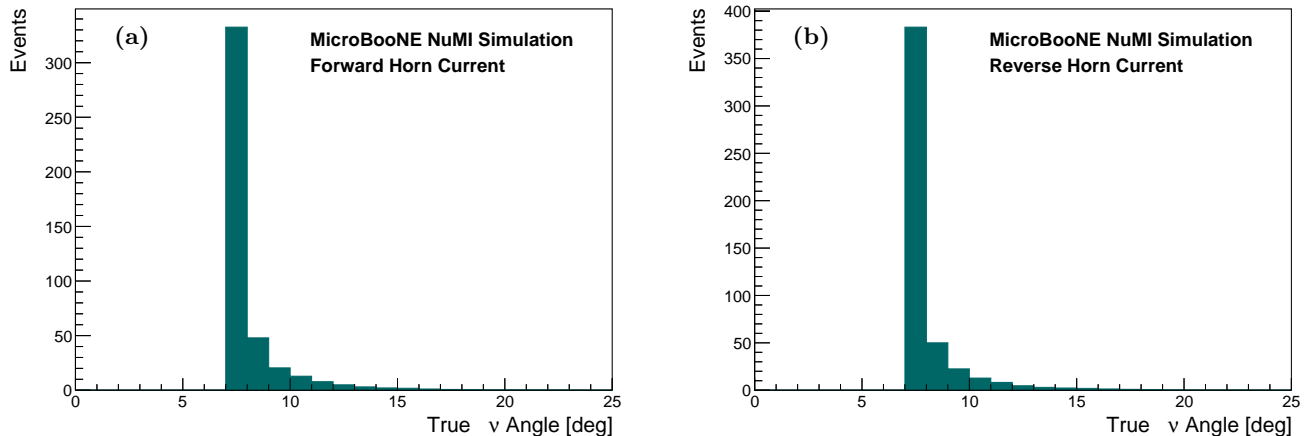


FIG. 2. Angular distribution of signal  $\bar{\nu}_e$  CC  $1\pi^\pm$  interactions for (a) FHC mode and (b) RHC mode.

During reconstruction the exact neutrino production position and, hence, direction is not known. Instead, the neutrino direction is approximated by assuming that the neutrino is produced at the NuMI target location approximately  $8^\circ$  off-axis from MicroBooNE. This provides an effective approximation for reconstructing angles  $\theta$  relative to the neutrino direction. For signal  $\bar{\nu}_e$  CC  $1\pi^\pm$  interactions, 85% have true neutrino directions within  $1^\circ$  of the approximated neutrino direction and 95% within  $3^\circ$  of the approximated neutrino direction.

For true  $\theta$  angles, the true neutrino direction is used rather than the approximation. The smearing resulting from the approximation is then accounted for during unfolding allowing the extracted cross-sections to be reported in terms of true  $\theta$  angles that are directly comparable with predictions of scattering angles from event generators. Figure 3 shows the smearing matrices for the electron angle,  $\theta_e$ , and pion angle,  $\theta_\pi$ , for the binning schemes considered. These encode the impact of the neutrino direction approximation along with other detector response and reconstruction effects on these variables. Greater than 75% of reconstructed angles fall within the correct truth bin for all bins considered indicating this approximation is performing well.

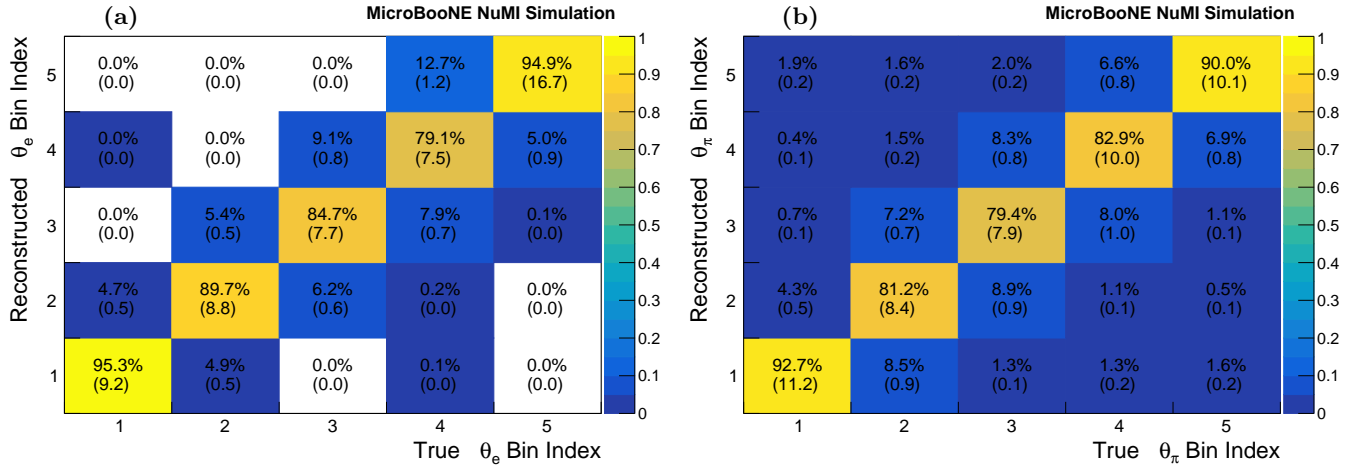


FIG. 3. Smearing matrices for (a) the electron angle,  $\theta_e$ , and (b) the pion angle,  $\theta_\pi$ , for the binning schemes considered. The number of predicted signal events in each bin is shown in parentheses.

## SELECTED EVENTS

Figure 4 shows the selected event distributions for the electron energy,  $E_e$ , electron angle,  $\theta_e$ , pion angle,  $\theta_\pi$ , and electron-pion opening angle,  $\theta_{e\pi}$ . Each distribution is divided by bin width. Good data-MC agreement is seen across all distributions within statistical and systematic uncertainties.

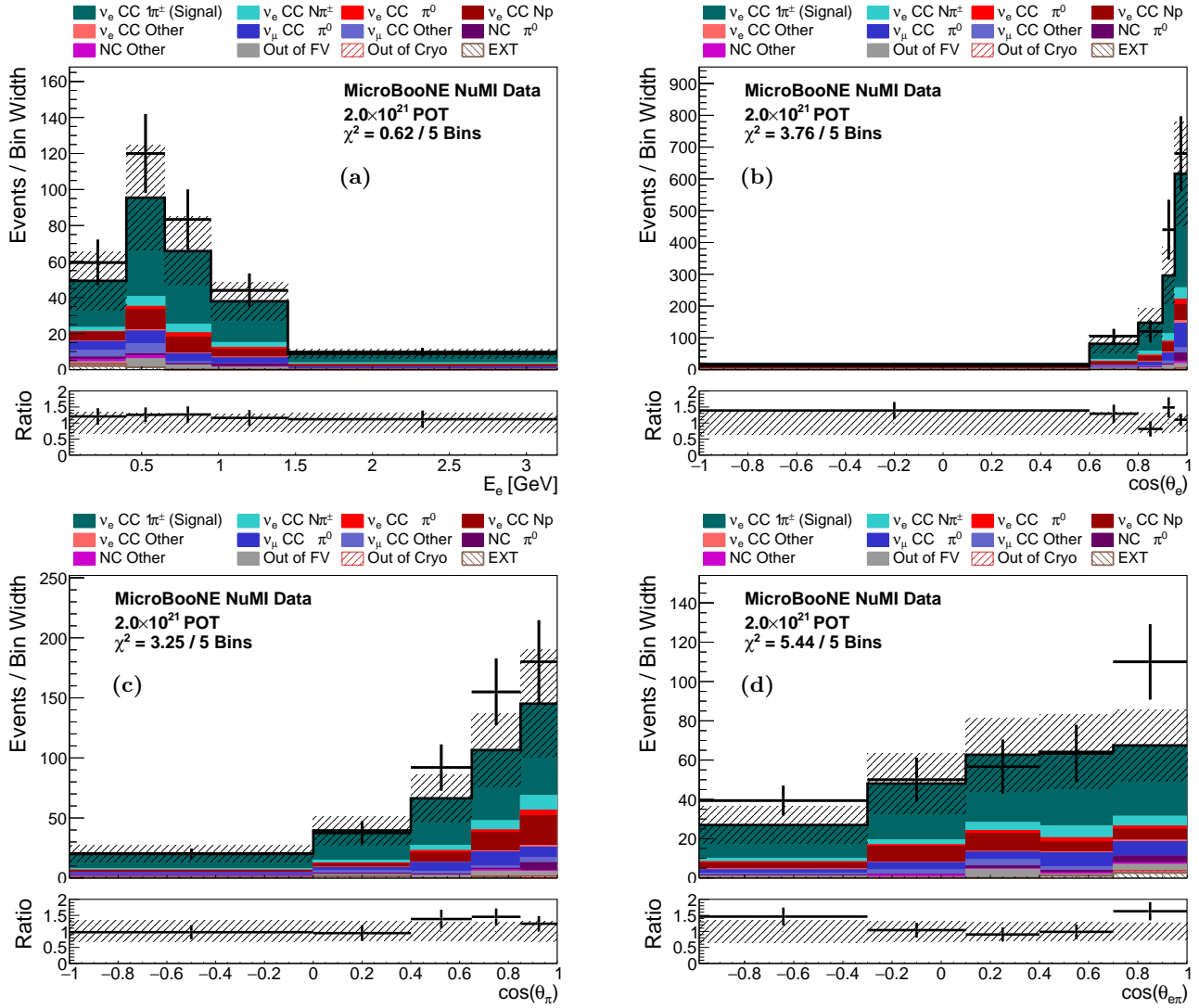


FIG. 4. Selected event distributions for (a) electron energy, (b) electron angle, (c) pion angle and (d) electron-pion opening angle. The shaded band shows the systematic and statistical uncertainty on the MC prediction and the black points show the data with statistical uncertainties.

## SIDEBANDS

Figure 5 shows the selected event distributions for the  $\pi^0$ -rich sideband in variables primary shower energy,  $E_{\text{Shower}}$ , primary shower angle,  $\theta_{\text{Shower}}$ , pion angle,  $\theta_\pi$ , and primary shower-pion opening angle,  $\theta_{\text{Shower}-\pi}$ . Each distribution is divided by bin width. Data-MC agreement within  $2\sigma$  is seen across all distributions within statistical and systematic uncertainties indicating the  $\pi^0$  background modeling is sufficient to proceed with cross-section extraction.

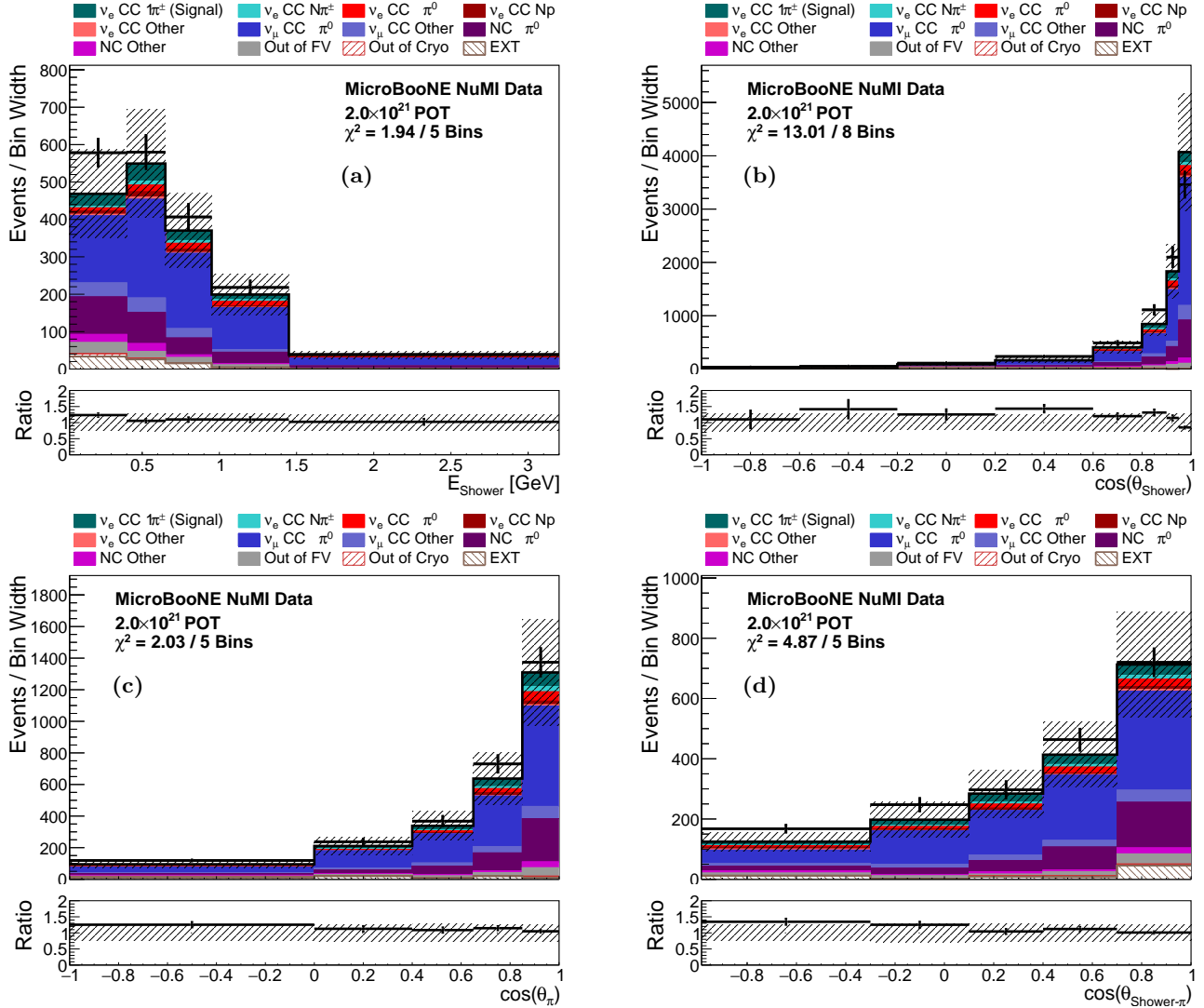


FIG. 5. Selected event distributions for the  $\pi^0$ -rich sideband in variables (a) primary shower energy, (b) primary shower angle, (c) pion angle and (d) primary shower-pion opening angle. The shaded band shows the systematic and statistical uncertainty on the MC prediction and the black points show the data with statistical uncertainties.

Figure 6 shows the selected event distributions for the  $\bar{\nu}_e$  CC  $Np$ -rich sideband in variables electron energy,  $E_e$ , electron angle,  $\theta_e$ , proton angle,  $\theta_p$ , and electron-proton opening angle,  $\theta_{ep}$ . Each distribution is divided by bin width. Data-MC agreement within  $2\sigma$  is seen across all distributions within statistical and systematic uncertainties indicating the  $\bar{\nu}_e$  CC  $Np$  background modeling is sufficient to proceed with cross-section extraction.

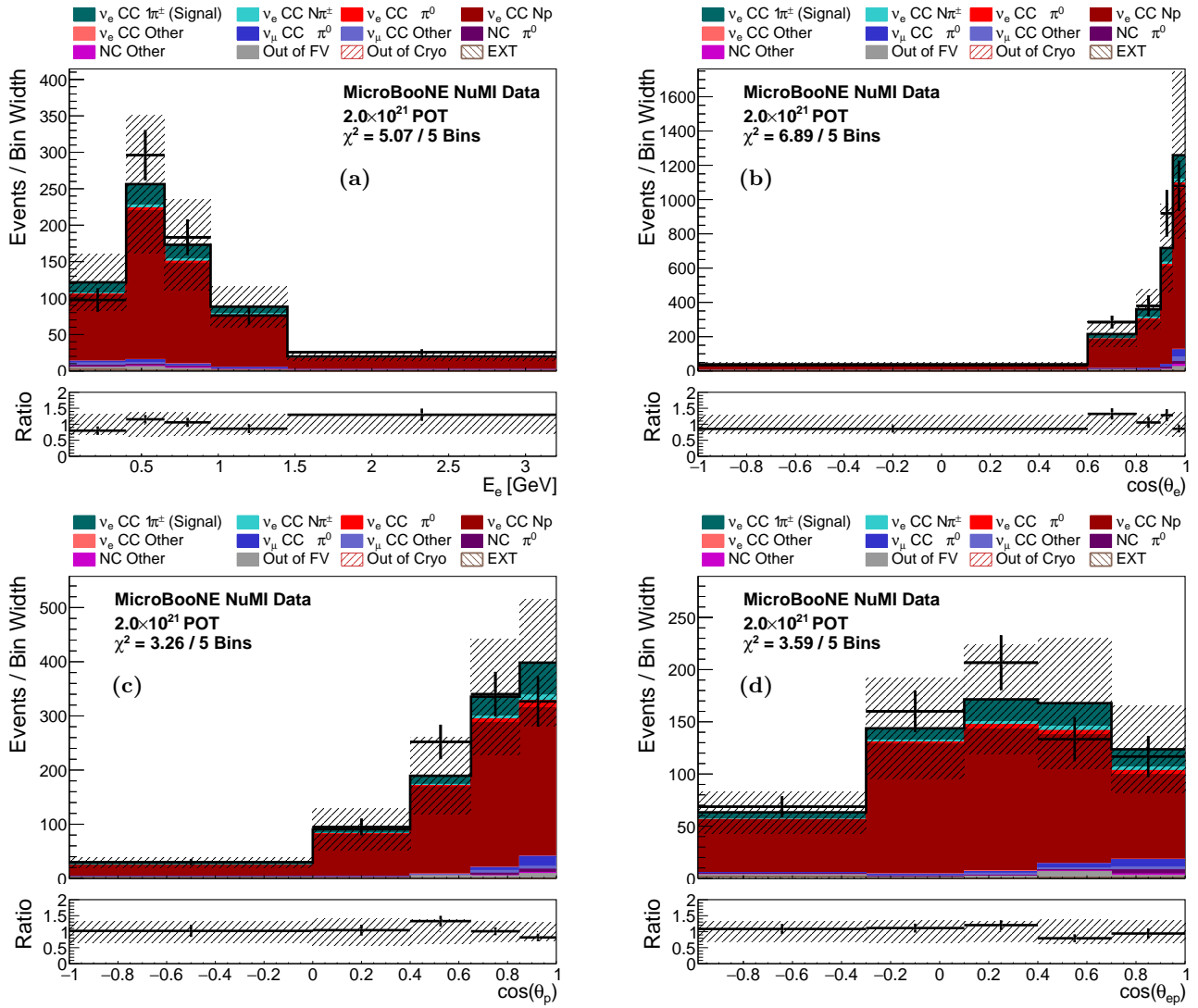


FIG. 6. Selected event distributions for the  $\bar{\nu}_e$  CC  $Np$ -rich sideband in variables (a) electron energy, (b) electron angle, (c) proton angle and (d) electron-proton opening angle. The shaded band shows the systematic and statistical uncertainty on the MC prediction and the black points show the data with statistical uncertainties.

## COVARIANCE AND CORRELATION MATRICES

Figures 7 and 8 show the total covariance and correlation matrices of the unfolded differential cross sections, respectively. These are evaluated using a block-wise unfolding technique allowing the correlations between variables to be reported [1]. The blocks are highlighted by the dashed lines and correspond to the electron energy (bins 1-5), the electron angle (bins 6-10), the pion angle (bins 11-15) and the electron-pion opening angle (bins 16-20).

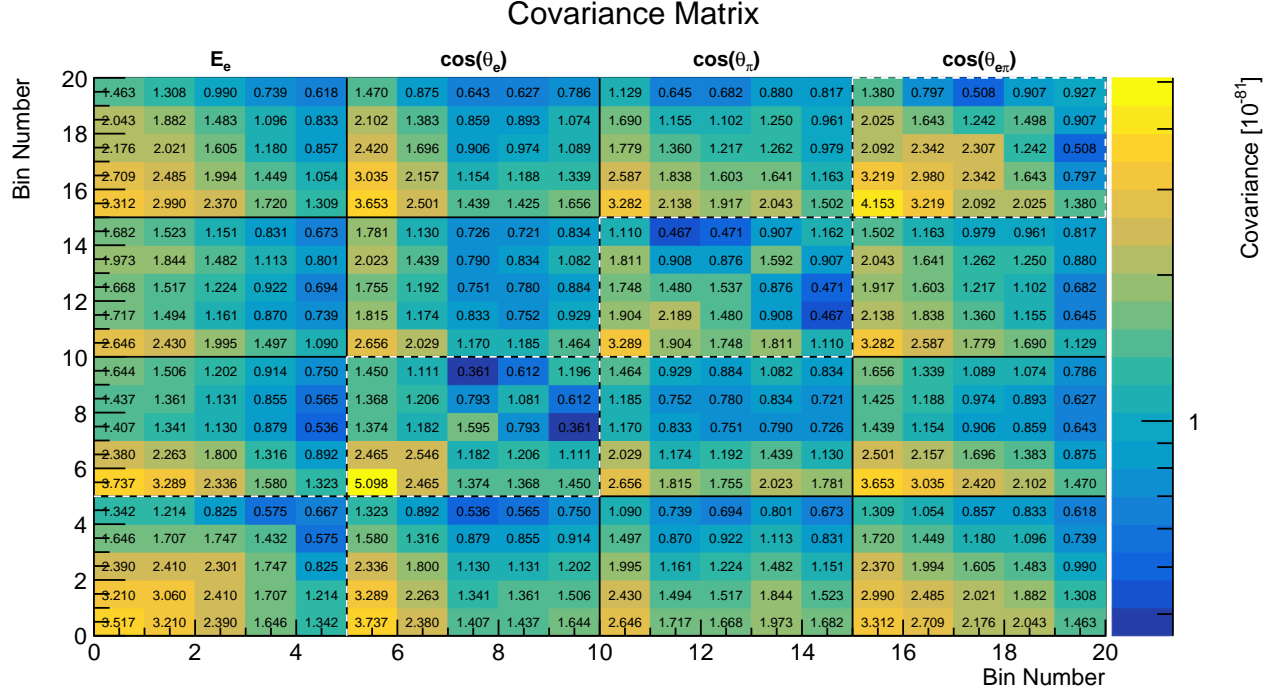


FIG. 7. Covariance matrix of the unfolded differential cross sections.

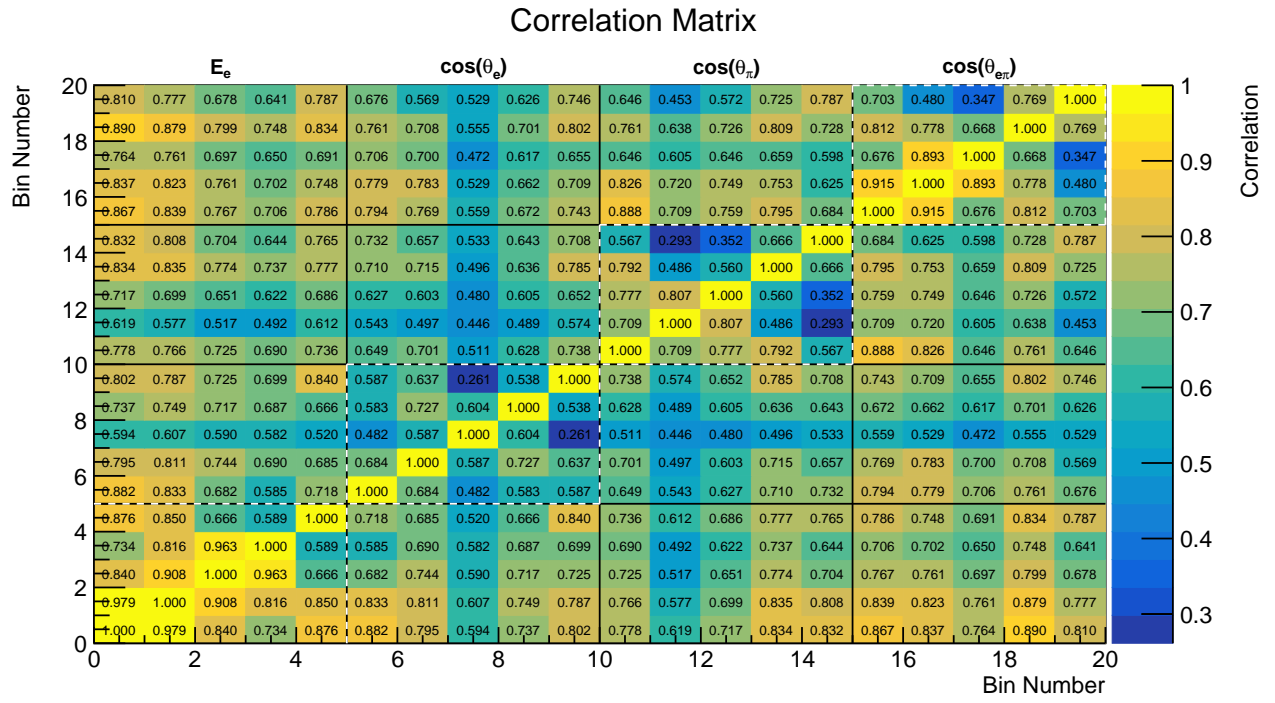


FIG. 8. Correlation matrix of the unfolded differential cross sections.



## REGULARIZATION MATRIX

Figure 9 shows the the regularization matrix that encodes the regularized truth space of the unfolded differential cross sections. This is reported with the same block structure as Figures 7 and 8. Since the unfolding is performed separately for each block there is no regularization between blocks [1]. Therefore, the off-block-diagonal terms in the regularization matrix are zero and not shown.

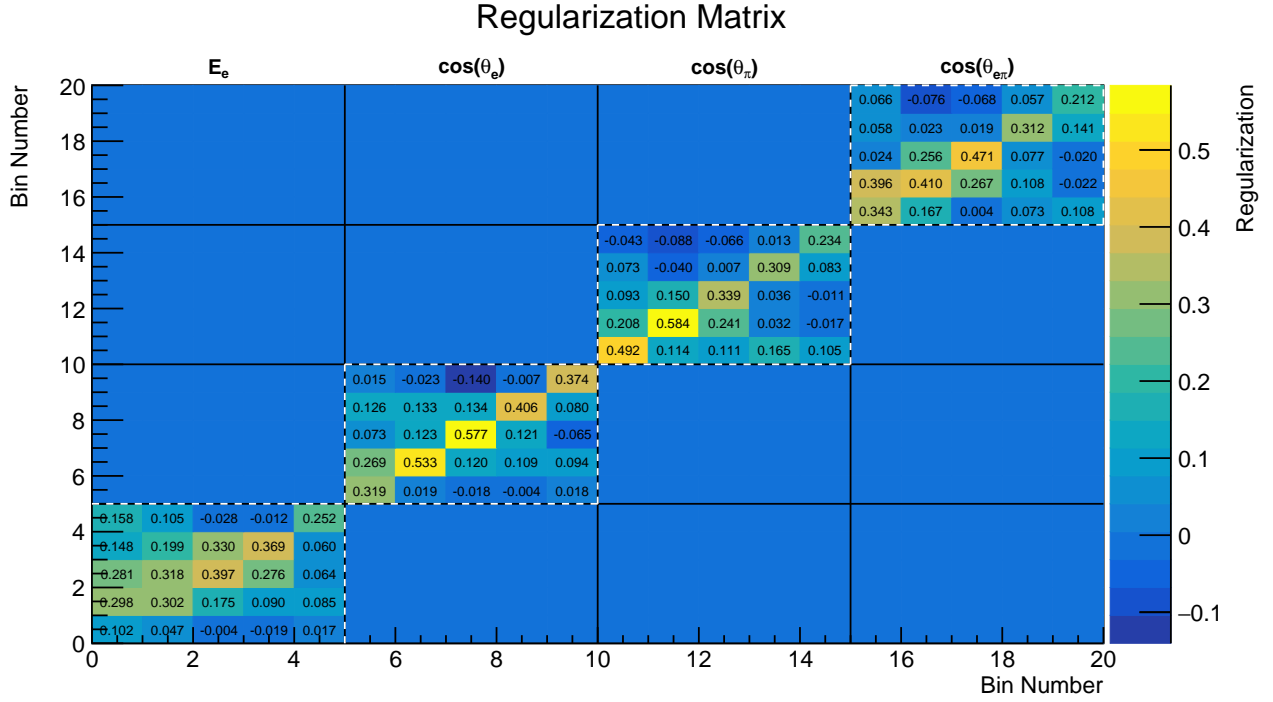


FIG. 9. Regularization matrix encoding the regularized truth space of the unfolded differential cross sections.

## DATA RELEASE

Tables I, II, III and IV summarize the unfolded results in regularized truth space. To compare these results with a theoretical prediction, the prediction must first be transformed into this regularized space by applying the regularization matrix. Additionally, the prediction should be divided by bin width. The data release with the data results, the covariance matrix, and the regularization matrix is included in the DataRelease.root file. Instructions on how to use the data release and the description of the binning scheme are included in the README file.

<b>Electron Energy, <math>E_e</math></b>					
Block Bin #	Global Bin #	Low Edge [GeV]	High Edge [GeV]	Cross Section [ $10^{-39}\text{cm}^2/\text{GeV}/\text{nucleon}$ ]	Uncertainty [ $10^{-39}\text{cm}^2/\text{GeV}/\text{nucleon}$ ]
1	1	0.03	0.40	0.487	0.160
2	2	0.40	0.65	0.680	0.221
3	3	0.65	0.95	0.472	0.160
4	4	0.95	1.45	0.211	0.076
5	5	1.45	3.20	0.041	0.014

TABLE I. Electron energy,  $E_e$ , unfolded cross section. The highest energy bin also serves as an overflow bin.

<b>Electron Angle, <math>\cos(\theta_e)</math></b>					
Block Bin #	Global Bin #	Low Edge	High Edge	Cross Section [ $10^{-39}\text{cm}^2/\text{nucleon}$ ]	Uncertainty [ $10^{-39}\text{cm}^2/\text{nucleon}$ ]
1	6	-1.00	0.60	0.129	0.045
2	7	0.60	0.80	0.650	0.252
3	8	0.80	0.90	0.475	0.399
4	9	0.90	0.95	1.897	0.658
5	10	0.95	1.00	1.886	0.692

TABLE II. Electron angle,  $\theta_e$ , unfolded cross section.

<b>Pion Angle, <math>\cos(\theta_\pi)</math></b>					
Block Bin #	Global Bin #	Low Edge	High Edge	Cross Section [ $10^{-39}\text{cm}^2/\text{nucleon}$ ]	Uncertainty [ $10^{-39}\text{cm}^2/\text{nucleon}$ ]
1	11	-1.00	0.00	0.119	0.057
2	12	0.00	0.40	0.178	0.117
3	13	0.40	0.65	0.365	0.157
4	14	0.65	0.85	0.572	0.200
5	15	0.85	1.00	0.583	0.227

TABLE III. Pion angle,  $\theta_\pi$ , unfolded cross section.

<b>Electron-pion Opening Angle, <math>\cos(\theta_{e\pi})</math></b>					
Block Bin #	Global Bin #	Low Edge	High Edge	Cross Section [ $10^{-39}\text{cm}^2/\text{nucleon}$ ]	Uncertainty [ $10^{-39}\text{cm}^2/\text{nucleon}$ ]
1	16	-1.00	0.00	0.280	0.094
2	17	0.00	0.40	0.273	0.136
3	18	0.40	0.65	0.199	0.160
4	19	0.65	0.85	0.322	0.129
5	20	0.85	1.00	0.373	0.101

TABLE IV. Electron-pion opening angle,  $\theta_{e\pi}$ , unfolded cross section.

---

[1] S. Gardiner, Mathematical methods for neutrino cross-section extraction, arXiv:2401.04065 [hep-ex] (2024).